

# A MINIATURE PHOSWICH DETECTOR FOR GAMMA-RAY LOCALIZATION AND BETA IMAGING

Martin P. Tornai\*, *Member, IEEE*, Craig S. Levin, *Member, IEEE*, Lawrence R. MacDonald, *Member, IEEE*, Clay H. Holdsworth, and Edward J. Hoffman, *Fellow, IEEE*

*Division of Nuclear Medicine & Biophysics, Department of Molecular & Medical Pharmacology, UCLA School of Medicine, Los Angeles, CA 90095*

## ABSTRACT

A combined  $\gamma$ -ray probe/ $\beta^+$  imaging detector was created by modification of a beta imaging intra-operative probe. This phoswich detector consists of a thin  $\text{CaF}_2(\text{Eu})$   $\beta^+$  imaging disk, coupled through a light diffuser to 7 or 19 parallelepiped high-Z scintillation crystals arranged hexagonally in columns. These elements are either  $2 \times 2 \times 10 \text{ mm}^3$  or  $4 \times 4 \times 10 \text{ mm}^3$  LSO, GSO or BGO crystals, and act as both light guides for the imaging light and as intrinsic  $\gamma$  detectors. The coincidence between the  $\text{CaF}_2(\text{Eu})$  and phoswich scintillators identifies  $\beta^+$  or true  $\beta^-$  events and suppresses accompanying annihilation or background  $\gamma$  events. The phoswich crystals are in turn coupled through optical fibers to a multi-channel PMT with positioning and discrimination electronics. Various characteristics of this novel imaging phoswich detector are investigated and presented for each of the phoswich combinations including: detector anisotropy, effects of time blocking and energy windows on phoswich imaging, intrinsic singles and phoswich spectral and spatial resolution characteristics, and phoswich imaging ability within  $\gamma$  background environments. The performance characteristics of the assembled prototype devices demonstrate that in surgery, this device can be used three ways: (1) rapid localization of  $\gamma$  emitting radionuclides with the modestly directional, self-collimated phoswich crystals; (2) high resolution  $\beta^-$  imaging or coarse (annihilation background corrupted)  $\beta^+$  imaging in singles mode; or (3)  $\beta^+$  imaging in coincidence mode with reduced  $\gamma$  background contamination.

## I. INTRODUCTION

More complete tumor resection has been shown to increase the life span and improve the quality of life of surgically treated patients [1,2]. This has been an underlying motivation in our development of beta [2-5] and gamma [2,3,6,7] sensitive imaging detectors. This class of intra-operative imaging detectors is designed to help delineate the remnant tumor boundaries which a surgeon could subsequently remove.

One anticipated high specificity, brain tumor radiotracer ( $^{18}\text{F}$ -fluorodeoxyuridine) emits positrons ( $\beta^+$ ) whose annihilation  $\gamma$ 's can also be imaged with PET. Direct  $\beta^+$  detection accompanied by 511 keV annihilation  $\gamma$  backgrounds in the patient's body, however, was previously shown to degrade image contrast [5]. Minimal  $\gamma$  background contributions were measured with low-Z, plastic scintillation detectors, but the more optimally beta efficient imaging detectors utilized somewhat higher Z  $\text{CaF}_2(\text{Eu})$  crystals [4,8-10]. A background count rate of  $\sim 1.5 \text{ cts/sec}/\mu\text{Ci}$  was measured with the  $\text{CaF}_2(\text{Eu})$  based imaging detector [5], which is approximately 5 times greater than the anticipated  $\beta^+$  count rate from the

\*Present address: Duke University Medical Center, Dept. of Radiology, DUMC-3949, Durham, NC 27710

exposed, labeled tumor tissue. Thus, it is necessary to reduce or eliminate the  $\gamma$  background contribution for this fiber-coupled, scintillator based imaging detector in order to produce artifact free images of the  $\beta^+$  distributions.

To accommodate artifact free  $\beta^+$  imaging, a novel position sensitive phoswich detector for intra-operative use is described. The principles of phoswich imaging were investigated, and various phoswich detector combinations implemented.

## II. BACKGROUND SUPPRESSION TECHNIQUES

### A. Phoswich Detector Configurations

Three techniques were considered to measure  $\gamma$  background contamination when detecting  $\beta^+$  distributions or for  $\gamma$  background suppression with  $\beta^-$  emitting nuclides with additional  $\gamma$  decay components (Fig. 1). The secondary  $\gamma$ -annular detector (Fig. 1, left) was previously investigated, and successfully imaged  $\beta^+$  distributions in background environments [5]. This configuration, however, has a poor detection efficiency, is somewhat cumbersome, and increases the overall size of the imaging detector, which may preclude using the device in small cavities. The second technique (Fig. 1, middle) which utilizes a phosphor sandwich technique, or phoswich [11], replaces the necessary light diffuser with a high-Z scintillator providing a large solid angle for detection of annihilation radiation. This technique also suffers from poor detection efficiency due to the required thinness of the phoswich scintillator (acting as the light diffuser) in order to obtain high spatial resolution from the imaging detector. Thus, the third technique (Fig. 1, right) combines the phoswich detector concept into a compact and efficient imaging

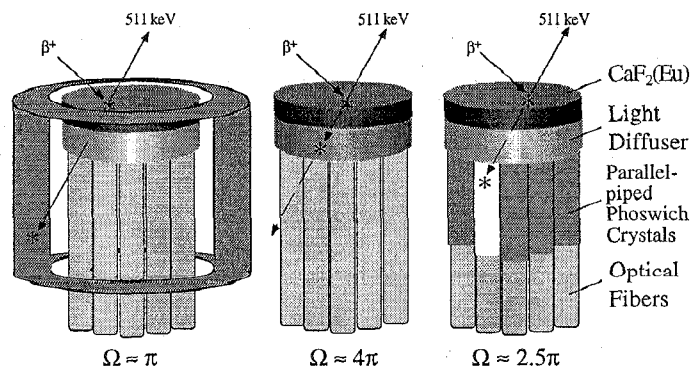


**FIGURE 1.** Conceptualization of three detection techniques. (Left) The ideal annular, coincident (and independent) detector is bulky. (Middle) Replacing the necessary light diffuser with a phoswich crystal suffers from inefficiency due to the detector thinness required for good spatial resolution from the adjunct imaging detector. (Right) There is a larger interaction probability with the phoswich detectors arranged in a columnar array; they act as both guides for the imaging light and as the phoswich detectors. ( $\Omega$  is the solid angle in steradians.)

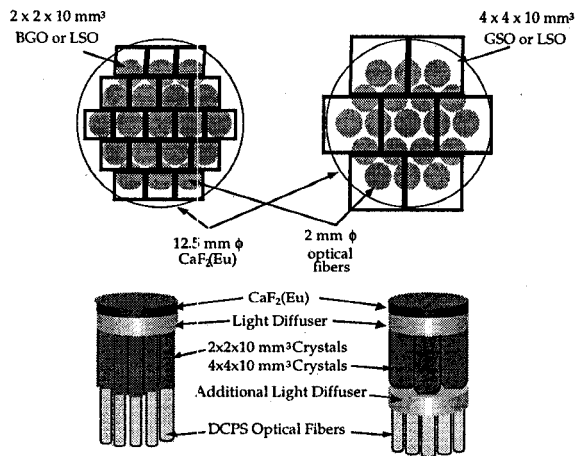


**FIGURE 2.** Top-down and perspective views of the coupling between the imaging  $\text{CaF}_2(\text{Eu})$  scintillator, light diffuser, square cross-section phoswich detectors, and round cross-section optical fibers in the hexagonal array. Black borders on crystals represent 3 layers of Teflon tape. DCPS = double clad, polystyrene.

detector which has a greater probability of detecting  $\gamma$ 's with its large volume and solid angle to the imaging detector. Other phoswich imaging devices have used columnar phoswich detectors [12-14] but not with this combination of imaging disk and columnar secondary (phoswich) detectors.

### B. Optical Coupling of Phoswich Components

High-Z and high density crystals were investigated for the proposed phoswich configuration along with the  $\text{CaF}_2(\text{Eu})$  ( $\lambda = 940$  nsec,  $I = 24$  k ph/MeV) imaging crystal. The parallelepiped crystals were highly polished on all surfaces. The available crystals were: BGO ( $\lambda = 300$  nsec,  $I = 8$  k ph/MeV), each  $2 \times 2 \times 10$  mm<sup>3</sup>; GSO ( $\lambda = 60$  nsec,  $I = 9.5$  k ph/MeV), each  $4 \times 4 \times 10$  mm<sup>3</sup>; LSO ( $\lambda \approx 40$  nsec,  $I = 28$  k ph/MeV), each either  $2 \times 2 \times 10$  mm<sup>3</sup> or  $4 \times 4 \times 10$  mm<sup>3</sup>.

The thickness of the necessary polystyrene light diffuser between the imaging  $\text{CaF}_2(\text{Eu})$  and the various phoswich crystals was chosen to minimize the uniformity variations for a flood field  $\beta^-$  irradiation. With the smaller BGO (and LSO) crystals, the light diffuser thickness was 2.1 mm (1.9 mm). For the larger GSO and LSO crystals, the light diffuser was  $\sim 4$  mm thick. At these thicknesses, the uniformity variations ( $\sigma < \pm 20\%$  pixel variation, with a mean pixel intensity of  $\sim 50$  cts) were a minimum, and the respective flood field images visually looked uniform. The necessary variation in light diffuser thickness is likely due to the different crystal refraction

indices and results in more optimal images.

The  $2 \times 2$  mm<sup>2</sup> phoswich crystal cross-sections match well with the 2 mm diameter ( $\phi$ ) double clad optical fibers used in the imaging probe [2-6], but the optical coupling was not ideal in these investigations (Fig. 2). Nevertheless, each of the smaller crystals in the array could be moderately well read out by the optical fibers. For the  $4 \times 4$  mm<sup>2</sup> cross-section crystals, an additional light diffuser was required in order to form an image of the crystal arrays, similar in concept to the unmatched, discrete crystal light sharing implementation employed with the gamma image probes [2,3,6].

## III. SIGNAL SEPARABILITY

### A. Preamplifier Time Constant

The separability of the scintillator combination can be easily achieved at the preamplifier stage of the electronic discrimination circuit. For short preamplifier time constants ( $\tau$ ), the signals with different decay times are more easily discriminated in time than with longer  $\tau$  [15]. The total signal (light output), however, depends on the integral of these calculable and measurable preamplifier response curves.

Thus, the integrals of the various phoswich scintillator preamplifier signals were compared to the integral  $\text{CaF}_2(\text{Eu})$  signal as a function of preamplifier  $\tau$ . Not surprisingly, the optimal calculated time constant occurs when the total light output ratio of the phoswich to  $\text{CaF}_2(\text{Eu})$  signal is maximized, which is near the decay time ( $\lambda$ ) of the faster phoswich scintillator ( $\tau_{\text{preamplifier}} \approx \lambda_{\text{faster}}$ ).

Measurements of the imaging PMT anode signal from the various phoswich combinations were made with  $\tau$  around the calculated optimal values. Each of the imaging scintillator phoswich combinations (as in Fig. 2) was independently irradiated with either  $^{204}\text{Tl}$  ( $\beta^- E_{\text{max}} = 765$  keV) or  $^{137}\text{Cs}$  (662 keV  $\gamma$ ) to discern the individual signals. The anode signal from the multi-channel (MC) PMT (*Philips XP1722*) (Fig. 6) was fed to a fast filter amplifier (*Ortec 579*) with various  $\tau$ ; the resultant time based pulses were digitized with a LabVIEW™ driven *Tektronix 2430* digital oscilloscope with GPIB connection to a *Macintosh IIfx*. The  $\lambda$  of the scintillators were extracted by fits to the measurements with the near optimal  $\tau = 50$  nsec (Fig. 3). The measured  $\lambda$ 's slightly over or underestimated the known values for the scintillators. This is in part because the measurements were made for a single event, and utilized only the most significant 8 bits in the 16 bit oscilloscope digitizer to minimize noise. Nevertheless, there was excellent separability between the signals.

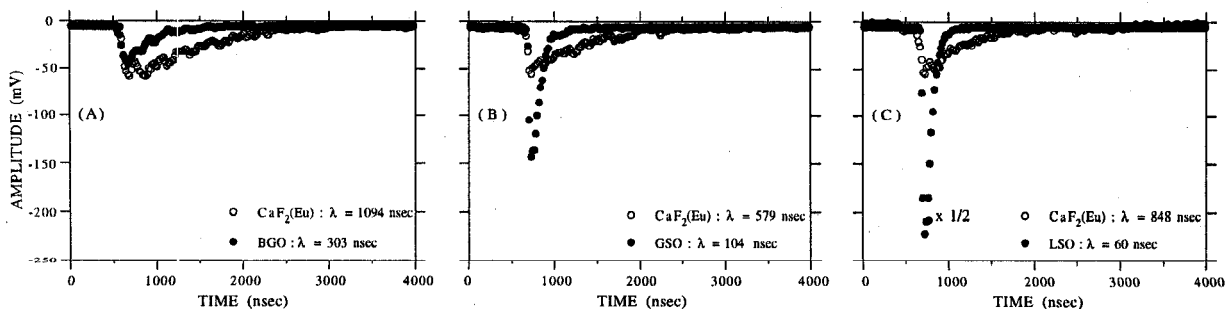


**FIGURE 3.** Measured digital oscilloscope signals from various phoswich crystal combinations of the Right set-up in Fig. 1. The phoswich detectors were irradiated with  $^{204}\text{Tl}$  betas, which only interact in the beta imaging detector, and  $^{137}\text{Cs}$  gammas which mainly interact in the high-Z phoswich detectors. Decay times were derived from fits to the data with the known preamplifier time constant.

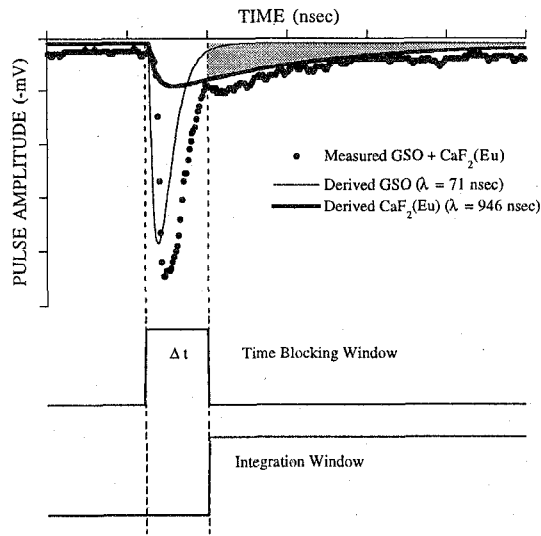


**FIGURE 4.** Oscilloscope signal of a single, simultaneous  $\beta^+$  and annihilation  $\gamma$  event measured with the  $\text{CaF}_2(\text{Eu})$  and GSO phoswich. The smooth curves are derived from parameter estimates from the simultaneous data. The first logic pulse overlaps the majority of the gamma portion of the simultaneous event, and blocks the faster portion of the signal from passing through a NC linear gate. The second logic corresponds in time to the integration window of the imaging portion of the signal.

### B. Time Blocking Window

Simultaneous  $\beta^+ + \gamma$  events were recorded with a point source of  $^{18}\text{F}$  on the  $\text{CaF}_2(\text{Eu})$  imaging surface with GSO phoswich (Fig. 4, top). The smooth curves in the figure were derived from fits of the double decay time spectrum of the simultaneous event. A coincidence is established between a  $\beta^+$  and  $\gamma$  event by imposing both an energy threshold and additional time threshold or time blocking window. If the energy threshold is set above the highest measured  $\text{CaF}_2(\text{Eu})$  only signal, which can be measured with the  $^{204}\text{Tl}$  pure  $\beta^-$  source as an analog to the  $^{18}\text{F}$   $\beta^+$  events, then only two types of events satisfy the energy threshold in the phoswich: (1) single  $\gamma$  events and (2) simultaneous  $\beta^+ + \gamma$  events. There is small probability that a  $\gamma$  event can scatter in the imaging detector and get stopped in the phoswich crystals, similar to condition (2). Events that interact only in the phoswich crystals (predominantly due to  $\gamma$  backgrounds) will trigger the gate but have no integrated imaging signal.

Given that the energy threshold in a discriminator is satisfied by an event, a time blocking window is triggered, as shown by the first logic pulse in Fig. 4. The blocking window size ( $\Delta t$ ) is affected by the combined signal amplitudes. The essential premise of the time blocking window is to screen out or block the non-imaging  $\gamma$  contribution from the imaging portion. A NIM linear gate module can be used to block portions of a signal (e.g. Fig. 6). If a signal passes through the linear gate, it will be integrated and shaped, as indicated by the second logic window. This technique is somewhat different than one which utilizes two time-to-digital converters of different time lengths (one short and one longer) to integrate the respective signals [16], but is similar in that two gates of different time duration are utilized to isolate the signal components. Additional spectroscopy information may be obtained when using two charge digitizers with different gate lengths in a phoswich device [12,16]. The longer charge

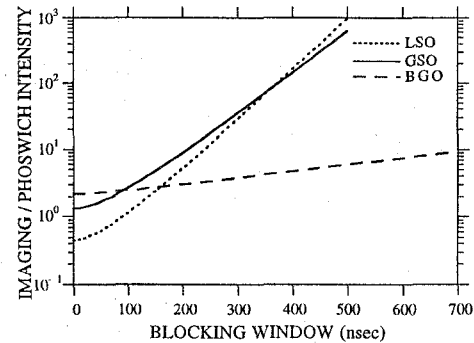


**FIGURE 5.** Ratio of the integrated  $\text{CaF}_2(\text{Eu})$  light to the integrated secondary phoswich scintillator light with increasing blocking window width. The phoswich scintillator light is normalized for a 511 keV deposition, while that for  $\text{CaF}_2(\text{Eu})$  is normalized for mean beta energies of 265 keV.

sensitive gate, however, may integrate considerable noise along with the real signal.

The effects of the time blocking window width, for a fixed  $\tau$  can be illustrated by numerical integration of the ideal component decay curves of the various scintillator combinations. It is not surprising that with larger  $\Delta t$ , the integrated signal decreases for imaging and phoswich scintillators. However, the ratio of the total imaging and phoswich signals with various  $\Delta t$  demonstrates that dimmer phoswich crystals may outperform brighter ones (Fig. 5). Since the amplitude and slope of this ratio are affected by the light output and  $\lambda$  of the phoswich scintillator, a fast, dim scintillator may be the ideal phoswich crystal in this application. Shorter time blocking windows could be used, thus preserving a greater portion of the imaging signal. This result is somewhat non-intuitive, yet still reflects the intrinsic characteristics of the scintillators employed.

### C. Electronic Circuit for Phoswich Imaging

The detected MC-PMT signals follow two pathways (Fig. 6). The MC-PMT anode signal combines the signals from the 19 optical fibers, regardless of the gain variations of any individual pixel signal. This is then filtered and linearly amplified before undergoing energy (CFD1) and timing discrimination (CFD2) with two constant fraction discriminators. Provided the anode signal satisfies the energy threshold, the resultant time blocking logic signal is split into four logic gates with the Fan-In-Fan-Out (FIFO) module which triggers a normally closed (NC) linear gate.

The 19 parallel imaging signals are passively gain balanced, resistively divided (multiplexed) and preamplified as shown on the lower pathway. A  $\tau = 51$  nsec ( $R = 510 \Omega \pm 5\%$  and  $C = 1000$  pF  $\pm 20\%$ ) was used on each of the Maxim 410 preamplifiers [2,4]. This value was considered more optimal for LSO and GSO than BGO, in combination with  $\text{CaF}_2(\text{Eu})$ . This is also considerably shorter than the  $\tau = 2$   $\mu\text{sec}$  previously reported for the  $\text{CaF}_2(\text{Eu})$  only, beta imaging probe. The NC linear gate passes all of the signal which does not correspond in time with the blocking window.

## IV. RAPID GAMMA LOCALIZATION

Utilizing the phoswich crystals in singles ( $\gamma$  only) mode adds functionality to the imaging detector. Thus the phoswich crystals could rapidly localize tumor hot spots based on proxi-

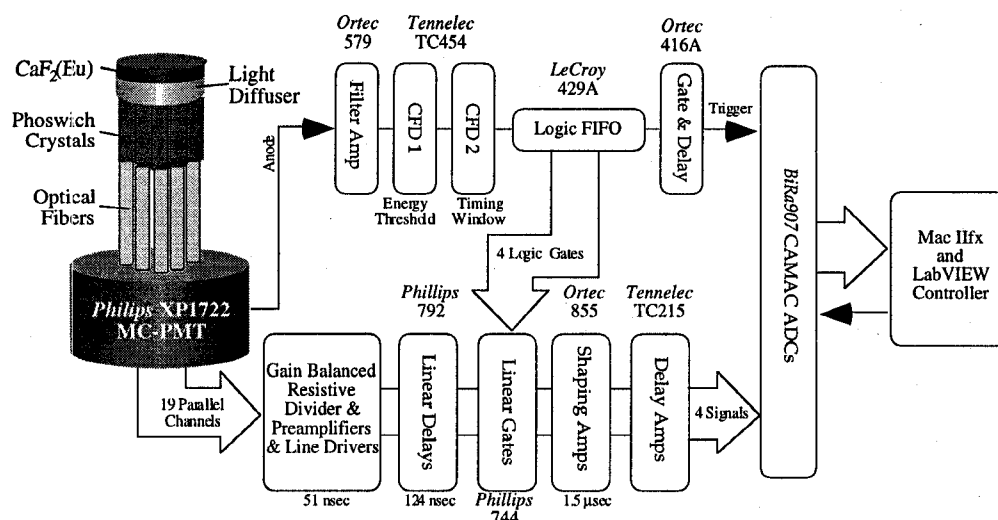


**FIGURE 6.** Electronic circuit for coincidence phoswich imaging. Detector is on the left. Upper pathway (NIM) provides energy and timing discrimination to validate coincident events; lower pathway (NIM) multiplexes and conditions signals for position decoding.

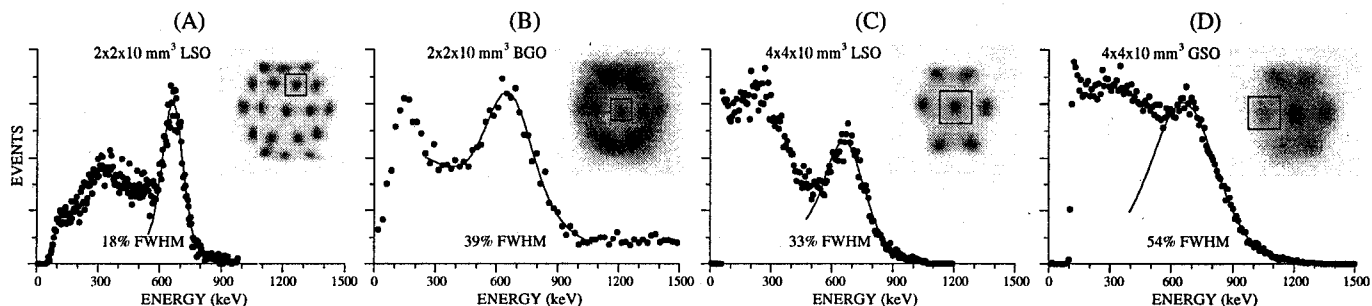


**FIGURE 7.** The singles  $^{137}\text{Cs}$  energy spectra from the various phoswich detectors: (A) 19 LSO elements, each  $2 \times 2 \times 10 \text{ mm}^3$ , (B) 19 BGO elements, each  $2 \times 2 \times 10 \text{ mm}^3$ , (C) 7 LSO elements, each  $4 \times 4 \times 10 \text{ mm}^3$ , (D) 7 GSO elements, each  $4 \times 4 \times 10 \text{ mm}^3$ . Inset images are the positioning flood histograms. Boundary regions in the images identify the crystal with the highest pulse height for which the energy spectra are plotted.

mity effects determined with count rate measurements. The crystals can be used as a self-collimated non-imaging  $\gamma$  ray detector, where the outer ring(s) of crystal elements act to shield the inner-most element of the phoswich array (Fig. 2).

### A. Energy Resolution Characteristics

The energy spectra and pulse heights for each phoswich crystal (Fig. 7) were extracted from crystal element look-up tables developed for these unique crystal coupling arrangements, but are similar in concept to those utilized for the discrete gamma imaging probes [2,3,6]. The BGO phoswich crystal regions were determined with the  $2 \times 2 \times 10 \text{ mm}^3$  element LSO crystals which were identical in size, but more easily distinguishable. A summary of the results for all the phoswich combinations is also given (Table 1).

Clearly, the higher light output LSO scintillator had overall better energy resolution and pulse height characteristics than either the BGO or GSO phoswich crystal arrays. However, it is not clear whether superior energy resolution is important in this phoswich application. One reason for the relatively poor energy resolution values is due to the non-optimal optical coupling between the phoswich detectors and optical fibers which conduct the signal to the remotely located MC-PMT (Fig. 2). Intrinsic detector and geometric efficiency are important in order to maintain a good sensitivity for the coincident gamma particles of interest, although detection by

**TABLE 1.** Measured intrinsic spectral resolution at 662 keV, and intrinsic spatial resolution measured with  $0.1 \text{ mm } ^{204}\text{Tl}$  beta slit source with the phoswich combinations. Y-Resolutions were not measured for the 7 element phoswich combinations.

Characteristic	19 Elements (each $2 \times 2 \times 10 \text{ mm}^3$ )		7 Elements (each $4 \times 4 \times 10 \text{ mm}^3$ )	
	LSO	BGO	LSO	GSO
Pulse Height (Mean $\pm \sigma$ %)	$100 \pm 20.3$	$19.4 \pm 3.6$	$57.4 \pm 11.8$	$30.5 \pm 8.5$
%FWHM (Mean $\pm \sigma$ %)	$21.1 \pm 6.13$	$65.4 \pm 24.0$	$39.4 \pm 5.10$	$66.0 \pm 13.5$
%FWHM Range	11.2 - 33.0	38.4 - 100.2	35.9 - 49.8	42.1 - 82.7
X-Resolution (FWHM $\pm \sigma$ mm)	$1.09 \pm 0.18$	$1.00 \pm 0.04$	$3.25 \pm 0.56$	$3.51 \pm 0.44$
Y-Resolution (FWHM $\pm \sigma$ mm)	$1.00 \pm 0.14$	$1.33 \pm 0.37$		

means of Compton scatter may be all that is required in order to produce a valid coincidence signal level. Knowledge of the energy resolution parameters are also important as a component to optimizing the threshold and time discrimination settings in the imaging phoswich detectors.

### B. Active Collimation and Detector Anisotropy

The outermost crystals can be used as an active shield for the innermost element (as depicted in Fig. 2). The information

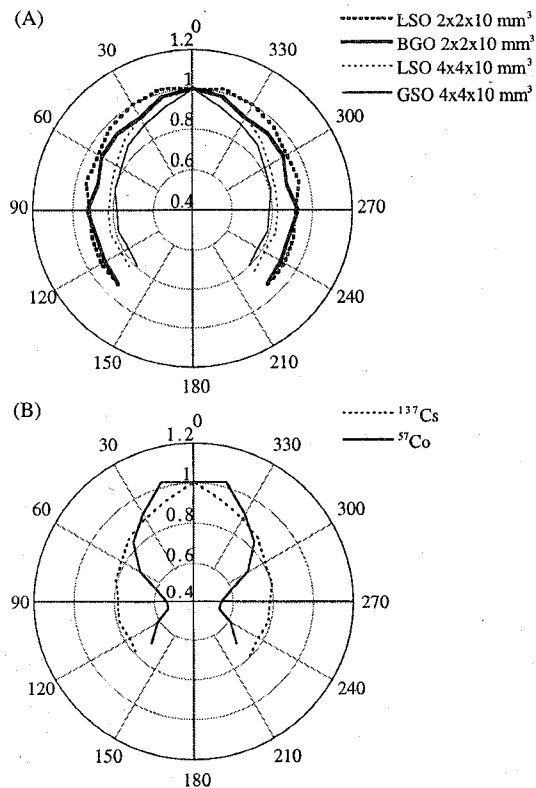


**FIGURE 8.** Directional anisotropy results for the relative sensitivity of the central crystal in (A) the various phoswich detector combinations irradiated from 2.5 cm distance with  $^{137}\text{Cs}$ , and (B) GSO phoswich irradiated with  $^{137}\text{Cs}$  and  $^{57}\text{Co}$  from the same distance. Note that with the less penetrating  $^{57}\text{Co}$   $\gamma$ 's, the measured anisotropy is enhanced as would be expected.

from the central most crystal can be digitally extracted (e.g. for the various energy spectra in Fig. 7). Then, by calculating the number of events in the central most crystal compared to the total number of energy windowed events collected for a fixed time, an estimate of the "sensitivity" of the central crystal to the source can be made. This solid angle argument relies on the efficiency change of the central most crystal with the different exposed area and detection efficiency of the outer rings of phoswich elements. The important parameter is the ratio of counts in the center to the total detected counts, which gives the magnitude of the sensitivity to a remote point source.

For all phoswich combinations, the anisotropy of the detector sensitivity to sources at various radial and azimuthal locations was measured with  $^{137}\text{Cs}$  and  $^{57}\text{Co}$  (122 keV) point sources held by a goniometer at fixed distances (2.5, 5 and 10 cm) from the center of the phoswich array and differing by  $15^\circ$  increments (Fig. 8). Due to the nature of the square crystals in the phoswich array, the anisotropy was not expected to be completely rotationally symmetric for all polar angles about the central axis of the phoswich array.

A window was placed over all of the crystal energy spectra, thus only the photopeak events were included in the calculation. While GSO has the lowest  $Z_{\text{eff}}$  and density of all the phoswich crystals, its sensitivity anisotropy response was the most pronounced (Fig. 8: a 20% effect from normal to a  $90^\circ$  azimuth). The strength of the anisotropy was considerably more pronounced at lower energy, as expected, due to the higher absorption of the  $\gamma$ 's in the outer active shield of the crystal array. Thus, not only would this phoswich detector be able to image  $\beta^\pm$  emissions in various backgrounds, but the device could be used to rapidly locate these lower energy  $\gamma$  sources, as is currently performed with non-imaging  $\gamma$  probes.

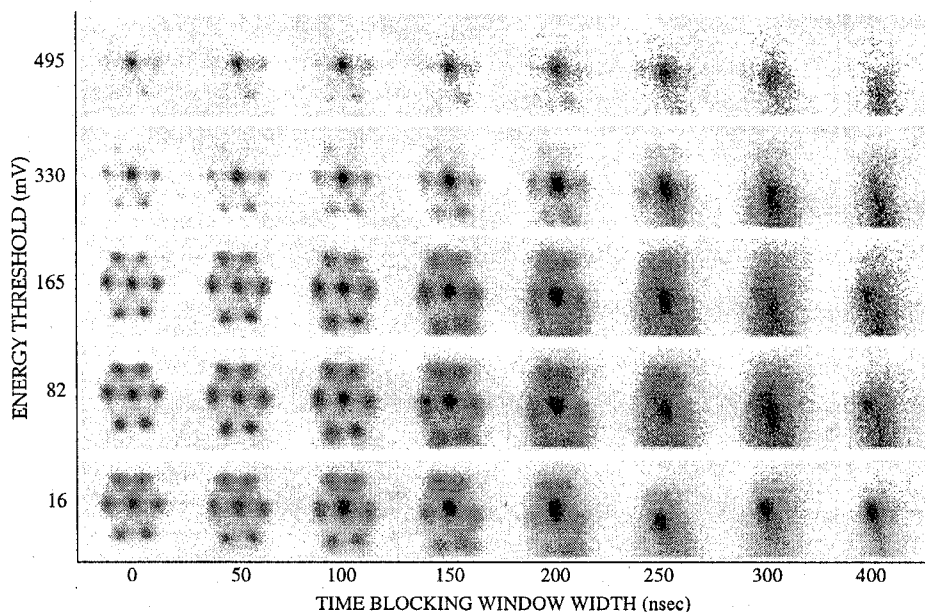


**FIGURE 9.** Resultant images of the variation in both energy threshold and time blocking window width for the  $4 \times 4 \times 10 \text{ mm}^3$  LSO crystal array phoswich. Measurement made with a 1 mm  $^{18}\text{F}$  point source on the detector surface. Each image is normalized to its own maximum intensity. Y-axis blurring with increasing time blocking is due to large noise in that dimension during the position decoding. The results for the other detectors are similar.

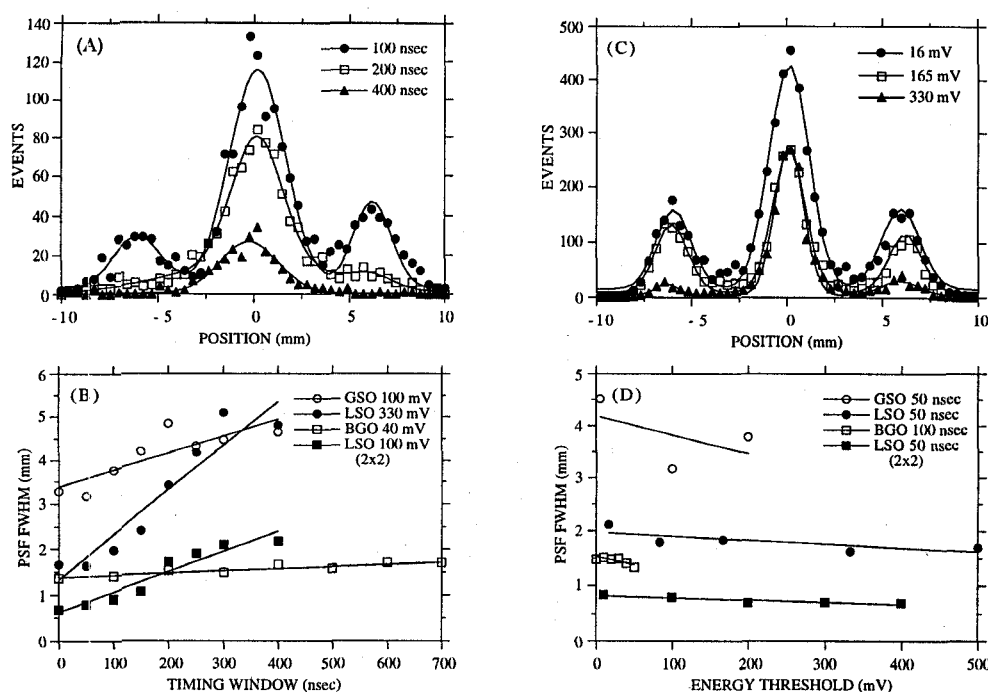


**FIGURE 10.** Characteristic measured PSF profiles, fit with triple Gaussian functions, made with the 1 mm  $^{18}\text{F}$  point source and (A) various timing windows for a nominal energy threshold with the GSO phoswich, and (C) various energy thresholds (indicated) for a 50 nsec fixed timing window with the 4x4x10 mm<sup>3</sup> LSO phoswich. Graphs (B) and (D) include the best results for combinations of timing window blocking and energy threshold PSF profiles in (A) and (C), respectively, as well as all other phoswich combinations.

## V. PHOSWICH IMAGING CHARACTERISTICS

### A. Intrinsic Spatial Resolution Performance

The intrinsic, non-coincidence spatial resolution was measured with a 0.1 mm black PMMA slit collimated  $^{204}\text{Tl}$  beta source stepped in 1.0 mm increments across the field of view of the various phoswich detector configurations (Table 1). For all cases with the LSO crystals, the natural background caused image artifacts. Thus, a long background acquisition, time normalized to the beta slit source acquisitions, was subtracted from the images and yielded a more uniform image in which the line source was more clearly distinguishable. Even with image normalization, hot spots were still apparent in the various images, but line spread function (LSF) profiles could still be measured from the image data.

### B. Variation of Threshold and Blocking Window

Using a 1 mm  $\phi$   $^{18}\text{F}$  source on the surface of a PMMA block, imaging measurements were made with the various phoswich configurations. The effects of the time blocking window width on the measured emission spatial resolution were characterized (Figs. 9 and 10A,B). As the length of the time blocking window is increased with a low energy threshold, less of the tail of the  $\gamma$  signal is integrated, suppressing the non- $\beta^+$  background (seen as detector element "spots" in the images and lobes in the point spread function (PSF) profiles). In addition, less of the  $\beta^+$  imaging signal is integrated, thus the spatial resolution degrades (Fig. 10B). This is also seen as a decreased PSF amplitude.

The cumulative effects of the time blocking window width and energy threshold on the measured emission spatial resolution were also characterized (Figs. 9 and 10C,D). As the energy threshold for a given time blocking window is

increased, only true  $\beta^+ + \gamma$  events satisfy the energy requirement, suppressing  $\gamma$  only events (also seen as lobes in the PSF profiles). This is more effective for the dimmer  $\gamma$  sensitive detectors. In addition, with higher thresholds, higher energy  $\beta^+$ s are selected (larger positioning pulse height), resulting in somewhat improved spatial resolution. For both the time blocking window and combined time blocking and energy threshold discrimination, the results with the near optimal thresholds are shown, and do not account for the finite source size or inherent  $\beta^+$  range in the holder or imaging detector.

### C. Preliminary Extrinsic Imaging Performance

The  $\text{CaF}_2(\text{Eu})/\text{BGO}$  phoswich was characterized in its ability to image a complex  $\beta^+$  emission phantom (Fig. 11) without and with various  $\gamma$  backgrounds. BGO was used as the phoswich crystal since it demonstrated good intrinsic spatial resolution characteristics and no intrinsic background signals. A resolution degradation was expected based on the intrinsic resolution values of the original  $\beta^+$  imaging probe [2,4] and measured characteristics of the phoswich probes.

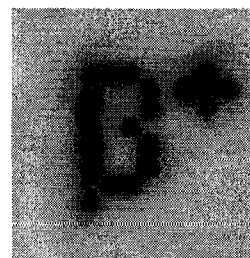


**FIGURE 11.** High resolution digital autoradiograph (25  $\mu\text{m}$  intrinsic FWHM resolution) of the  $^{18}\text{F}$  filled  $\beta^+$  emission phantom. Total volume is  $\sim 4$   $\mu\text{L}$  in the 21 element 0.5 mm  $\phi$  wells in PMMA, spaced on 0.6 mm horizontal and vertical pitch.

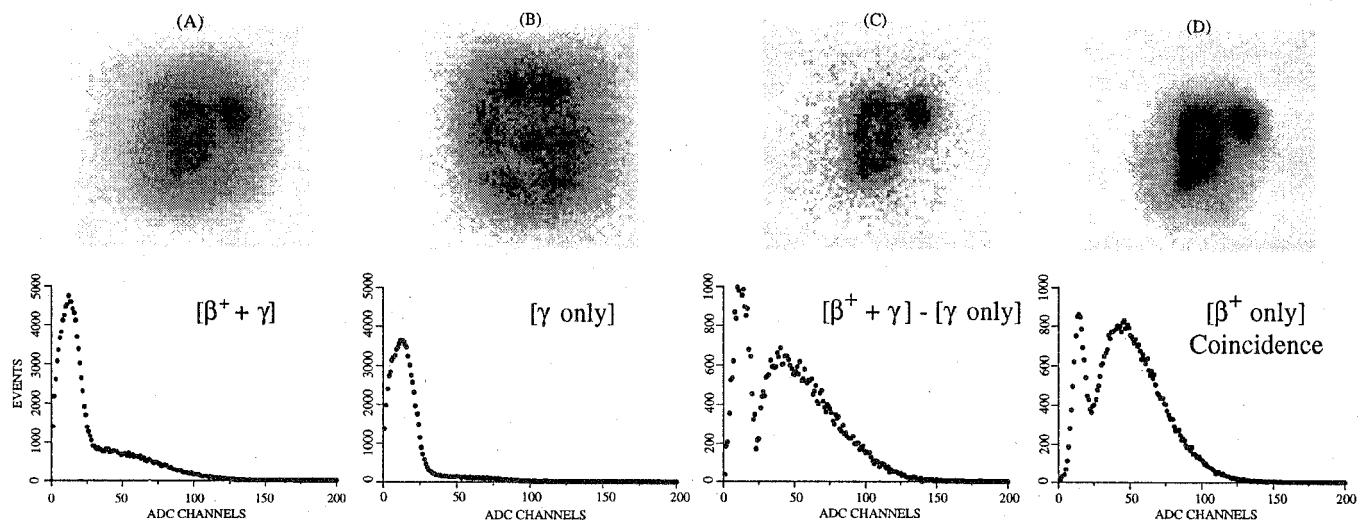


**FIGURE 12.** Resultant images and respective energy spectra of the  $\beta^+$  emission phantom on the BGO phoswich. (A) Measurement without any background rejection (no energy or timing thresholds) includes both  $\beta^+$  and  $\gamma$ 's; (B) measurement of the  $\gamma$  component by shielding the  $\beta^+$  with a 0.4 mm thin Cu plate; (C) the difference image and spectrum of (A) - (B); (D) coincidence image with 100 nsec time blocking window and 50 mV threshold. There are  $\sim 4\times$  higher statistics in (D) than in (C), and the respective energy spectra were count normalized.

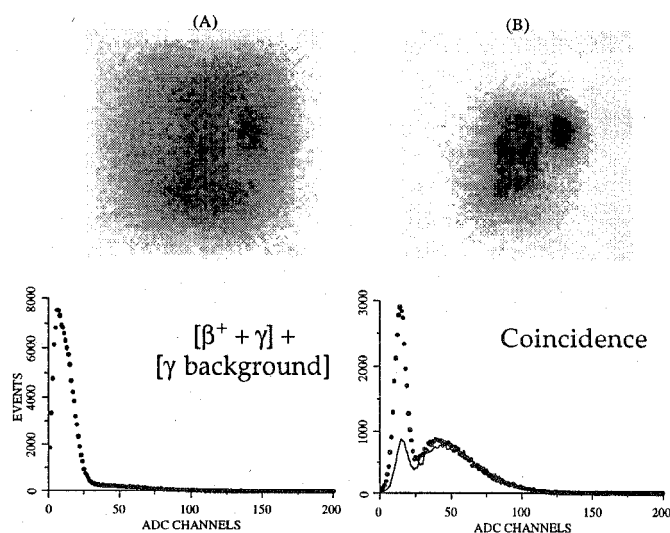


**FIGURE 13.** Measurements made with the BGO phoswich as in Fig. 12 but with an additional 250  $\mu\text{Ci/L}$   $^{18}\text{F}$  (511 keV  $\gamma$  source) activity in 400 mL water directly behind the  $\beta^+$  emission phantom. Measurements made (A) without and (B) with background rejection with the 50 mV and 100 nsec time blocking thresholds. Spectral data in (B) includes the spectra from Fig. 12D (solid line) to illustrate the increased gamma component in the lower energy portion of the spectrum due to the added  $\gamma$  background.

Qualitatively, the phoswich imaging result is similar to the difference between the  $[\beta^+ + \gamma]$  and  $[\gamma\text{-only}]$  images (Fig. 12), which is considered a good reference [5]. The timing window width and energy threshold utilized were based on the results in Fig. 10. There are  $\sim 4$  times more statistics in the phoswich image compared to the difference image (Fig. 12), yet there is a 45% reduction in overall acquisition time with the implemented phoswich to achieve an image with similar statistical properties as the difference image. The large solid angle between the imaging crystal and phoswich scintillators,

and the fact that only a single measurement need be made helps reduce the overall imaging time.

The count normalized energy spectra also have qualitatively similar features. While not a clear photopeak, the low energy peak (Figs. 12C,D) is due to gamma contamination. This is based on the features and trends observed from the singles and coincidence energy spectra of the various phoswich configurations, as a function of timing window width and energy threshold. The  $\beta^+$  component is the larger, higher energy continuum spectrum. While the peak counts in the gamma to beta spectra are 5:3 in the difference image, they are nearly 1:1 in the phoswich implemented image. This indicates that there is less  $\gamma$  contamination in the phoswich implementation compared to the simple subtraction of two measurements.

#### D. Background Elimination with Phoswich Imaging

To determine if the phoswich device will work in an environment with a high  $\gamma$  background flux, a 400 ml container with  $^{18}\text{F}$  activity was placed immediately behind the emission phantom. With the background activity, the imaging phoswich detector extracted the  $\beta^+$  signal, but with a noticeably increased  $\gamma$  contribution in the lower energy peak (Fig. 13). The energy spectrum without background is included for comparison. Note that the  $\gamma$  to  $\beta^+$  peak counts are now approximately 3:1 while the ratio of the background activity to emission phantom activity is nearly  $10^4$ . Thus, while there is some  $\gamma$  contamination in the image and energy spectrum, the true emission distribution is nevertheless identifiable. Moreover, an additional low energy threshold on the energy spectrum will eliminate background events further.

## VI. CONCLUSIONS

These initial experiments validate the utility of this novel phoswich imaging probe for  $\beta^{\pm}$  imaging corrupted by  $\gamma$  backgrounds or annihilation radiation. This device combines various aspects of the intrinsic beta imaging and gamma imaging intra-operative probes previously investigated. Thus,

this device can realistically be used as a  $\beta^-$  or  $\beta^+$  imaging device, and can be further utilized as a modestly directional  $\gamma$  detector for rapid localization of remote sources of different energies. The detector assemblies had  $\sim 1$  mm intrinsic spatial resolution and could resolve complex  $\beta^+$  emission phantoms whose  $2\pi$  emission and beta range causes additional resolution blurring. The implemented BGO phoswich extracted the true  $\beta^+$  signal with an additional high flux  $\gamma$  background which simulated the surgical scenario.

Improvements can be made in the final imaging device. It was shown that dim and fast phoswich scintillators should perform better than brighter ones. Thus GSO may be a more suitable candidate than LSO, which is very bright, and is faster than BGO with which the imaging measurements were performed. Nevertheless, the BGO device produced recognizable images which could be distinguished from within background environments. A more optimal cylindrical scintillator geometry as well as better optical coupling with the fibers would also improve the imaging and energy performance. With modest changes to the front-end entrance window, the device developed in this paper could be adapted for high resolution alpha particle imaging as well [17].

These more optimal beta imaging devices need to be tested in realistic environments to validate their effectiveness for *in situ* use.

#### ACKNOWLEDGMENTS

The authors thank Drs. S. Cherry and M. Dahlbom for use of the LSO, BGO and GSO crystals, Dr. S. Majewski for helpful discussions, K. Meadors and D. Kim for expert technical assistance, and Dr. G. Clark for the use of his digital oscilloscope. This work was funded in part by NIH/NCI grants R01-CA61037, T32-CA09092, DOE contract DE-FC03-87-ER60615.

#### REFERENCES

- [1] M Ammirati, N Vick, YL Liao, *et al.* 1987. Effect of the Extent of Surgical Resection on Survival and Quality of Life in Patients with Supratentorial Glioblastomas and Anaplastic Astrocytomas. *Neurosurgery*. **21**(2): 201-206.
- [2] MP Tornai. 1997. *Small Area Beta and Gamma Detectors for Functional Nuclear Emission Imaging*. UCLA. Ph.D. Thesis, and references therein.
- [3] EJ Hoffman, MP Tornai, CS Levin, *et al.* 1997. Gamma and Beta Intra-Operative Probes. *Nucl. Instr. Meth.* **A389**:324-329.
- [4] MP Tornai, LR MacDonald, CS Levin, *et al.* 1996. Design Considerations and Initial Performance of a 1.2  $\text{cm}^2$  Beta Imaging Intra-Operative Probe. *IEEE Trans. Nucl. Sci.* **NS-43**(4):2326-2335.
- [5] CS Levin, MP Tornai, LR MacDonald, EJ Hoffman. 1997. Annihilation  $\gamma$  Ray Background Characterization and Rejection for a Small Beta Camera Used for Tumor Localization During Surgery. *IEEE Trans. Nucl. Sci.* **NS-44**(3):1120-1126.
- [6] MP Tornai, CS Levin, LR MacDonald, EJ Hoffman. 1997. Investigation of Crystal Geometries for Fiber Coupled Gamma Imaging Intra-Operative Probes. *IEEE Trans. Nucl. Sci.* **NS-44**(3):1254-1261.
- [7] BE Patt, JS Iwanczyk, MP Tornai, *et al.* 1997. Development of an Intraoperative Gamma Camera Based on a 256-Pixel Mercuric Iodide Detector Array. *IEEE Trans. Nucl. Sci.* **NS-44**(3):1242-1248.
- [8] CS Levin, LR MacDonald, MP Tornai, EJ Hoffman, J Park. 1996. Optimizing Light Collection from Thin Scintillators Used in a Beta-Ray Camera for Surgical Use. *IEEE Trans. Nucl. Sci.* **NS-43**(3):2053-2060.
- [9] MP Tornai, EJ Hoffman, LR MacDonald, CS Levin. 1996. Characterization of Fluor Concentration and Geometry in Organic Scintillators for *in Situ* Beta Imaging. *IEEE Trans. Nucl. Sci.* **NS-43**(6):3342-3347.
- [10] S Yamamoto, C Seki, K Kashikura, *et al.* 1997. Development of a High Resolution Beta Camera for a Direct Measurement of Positron Distribution on Brain Surface. *IEEE Trans. Nucl. Sci.* **NS-44**(4):1538-1542.
- [11] DH Wilkinson. 1952. The Phoswich - A Multiple Phosphor. *Rev. Sci. Instr.* **23**(8):414-417.
- [12] M Bantel, RG Stokstad, YD Chan, *et al.* 1984. A Two-Dimensional Position Sensitive Phoswich Detector. *Nucl. Instr. Meth.* **226**: 394-404.
- [13] Z He, D Ramsden. 1993. A Broad-Band Position Sensitive Phoswich Detector for Gamma-Ray Astronomy. *Nucl. Instr. Meth.* **A336**:330-335.
- [14] M Dahlbom, LR MacDonald, L Erikson, *et al.* 1997. Performance of a YSO/LSO Detector Block for Use in a PET/SPECT System. *IEEE Trans. Nucl. Sci.* **NS-44**(3):1114-1119.
- [15] GF Knoll. 1979. *Radiation Detection and Measurement*. John Wiley & Sons, Inc. New York.
- [16] DA Cebra, WK Wilson, AV Molen, GD Westfall. 1992. The Light Response of Plastic Scintillators and the Calibration of Large Arrays. *Nucl. Instr. Meth.* **A313**:367-372.
- [17] S Yamamoto, T Iida, I Kanno. 1997. Development of a High Resolution Alpha Camera. *Nucl. Instr. Meth.* **A392**:291-294.